Shuai He, Ching-Tai Ng, Carman Yeung

Time-Domain Spectral Finite Element Method for Modeling Second Harmonic Generation of Guided Waves Induced by Material, Geometric and Contact Nonlinearities in Beams

International Journal of Structural Stability and Dynamics, 2020; 20(10)© World Scientific Publishing Company 2020

Journal article:

Shuai He, Ching Tai Ng, Carman Yeung. (2020). Time-domain spectral finite element method for modelling second harmonic generation of guided waves induced by material, geometric and contract nonlinearities in beams. International Journal of Structural Stability and Dynamics, 20(10):2042005.

Time-domain spectral finite element method for modeling second harmonic generation of guided waves induced by material, geometric and contact nonlinearities in beams

Shuai He
School of Civil, Environmental & Mining Engineering,
The University of Adelaide University,
Adelaide, SA 5005, Australia
shuai.he@adelaide.edu.au

Ching-Tai Ng[1]
School of Civil, Environmental & Mining Engineering,
The University of Adelaide University,
Adelaide, SA 5005, Australia
alex.ng@adelaide.edu.au

Carman Yeung
School of Civil, Environmental & Mining Engineering,
The University of Adelaide University,
Adelaide, SA 5005, Australia
carman.yeung@adelaide.edu.au

Abstract

This study proposes a time-domain spectral finite element (SFE) method for simulating the second harmonic generation (SHG) of nonlinear guided wave due to material, geometric and contact nonlinearities in beams. The time-domain SFE method is developed based on the Mindlin-Hermann rod and Timoshenko beam theory. The material and geometric nonlinearities are modeled by adapting the constitutive relation between stress and strain using a second order approximation. The contact nonlinearity induced by breathing crack is simulated by bilinear crack mechanism. The material and geometric nonlinearities of the SFE model are validated analytically and the contact nonlinearity is verified numerically using three-dimensional (3D) finite element (FE) simulation. There is good agreement between the analytical, numerical and SFE results, demonstrating the accuracy of the proposed method.

[1] Corresponding Author

Numerical case studies are conducted to investigate the influence of number of cycles and amplitude of the excitation signal on the SHG and its performance in damage detection. The results show that the amplitude of the SHG increases with the numbers of cycles and amplitude of the excitation signal. The amplitudes of the SHG due to material and geometric nonlinearities are also compared with the contact nonlinearity when a breathing crack exists in the beam. It shows that the material and geometric nonlinearities have much less contribution to the SHG than the contact nonlinearity. In addition, the SHG can accurately determine the crack location without using the reference data. Overall, the findings of this study help further advance the use of SHG for damage detection.

Keywords: Nonlinear guided waves, second harmonic, spectral finite element, material nonlinearity, geometric nonlinearity, contact nonlinearity, breathing crack

1 Introduction

Structural health monitoring (SHM) has attracted increasing attention in the last two decades as it has played a vital role in maintaining the structural safety and serviceability in civil, aerospace and mechanical engineering. Different techniques were developed to provide early damage detection in structures. For example, conventional non-destructive evaluation (NDE) techniques, such as visual inspection, eddy current [1] and ultrasonic technique [2, 3], were developed to provide offline inspection of the structural integrity. However, the majority of the NDE techniques are not suitable for online and in-situ monitoring of the structures due to the sustainability of transducers and cost issues. Most NDE techniques are not applicable to inspect inaccessible location of the structures. They are costly, time consuming, and under manual operation according to schedule maintenance cycles. Vibration based approach is the other commonly used damage detection technique [4-6]. This method concerns the variation in physical properties, such as mass, stiffness and damping. And these properties directly affect the values of modal parameters, like natural frequencies and mode shapes [7]. For instance, cracks will be identified if there is an indication of the stiffness reduction. However, there are two reasons limiting the application of this technique to detect damage in practice. The first limitation is that significant damage usually causes very small changes in the modal parameters. The other one is the change of modal parameters caused by damage may be undetected due to the varying environmental and operational condition.

1.1 Linear guided waves

The other approach that has attracted significant attention is based on guided waves to evaluate the integrity of structures. Guided waves are mechanical stress waves which propagate along the structure are guided by the boundaries of the structures. They propagate at high speeds, up to thousand m/s. Guided waves could be used for in-situ monitoring of relatively large area of the structure. In other words, this technique is good for long-range inspection. Different techniques were developed to employ the guided waves for damage detection of different types of structures, such as beam [8, 9], pipe [10] and metallic plate [11-13] and composite materials [14, 15]. The damage detection is achieved by the change of the characteristics of the guided wave responses at the same frequency of the input signal. But this technique is only effective when the damage size is similar or larger to the wavelength of the guided waves. The majority of the techniques based on the linear guided waves require reference (baseline) data when the structure is intact to extract the information of the damage from the measured signals. However, the stability of the baseline data is significantly affected by the varying temperature [16] and operational condition [17-19].

To achieve early detection of damage, nonlinear features of guided waves, such as higher harmonics [20-22], sub-harmonics [23, 24], shift of resonance frequency [25] and mixed frequency response [26], have been used for damage detection. Specifically, the generation of higher harmonics, which frequencies are in multiple times of the input signal frequency, has been widely used as an indicator for early detection of damages. Compared to the linear features of guided waves, the nonlinear features are more sensitive to the micro-structural change and less influenced by varying temperature and operational condition of the structures.

1.2 Nonlinear features of guided waves

Early research into nonlinear guided waves focused on the bulk waves and Rayleigh surface waves [27]. Different from bulk waves and Rayleigh surface waves [28], the guided waves can be highly dispersive if it is generated using inappropriate excitation frequency. Guided waves generally contain multiple wave modes and their group and phase velocities usually vary with frequency. To effectively utilize the nonlinear guided waves, different studies have investigated the conditions on the cumulative second harmonic generation (SHG) of guided wave, such as internal resonance, group velocity matching and guided wave modes interaction [29]. The results showed that under such conditions the detectability of the higher harmonics in nonlinear guided wave could be improved significantly.

Higher harmonic generated [30] due to the nonlinearities existed in the structures, which are attributed to material behaviour, geometry, structural joints and damage. For an undamaged isotropic homogeneous solid medium, geometric nonlinearity and material nonlinearity can distort the passing guided waves to induce the higher harmonics. The geometric nonlinearity is due to the finite deformation of the structures. The material nonlinearity is mainly generated by the discontinuity of the medium at lattice level, i.e. imperfections in atomic lattices. The effect of higher harmonic generation is enhanced when there are additional imperfections in medium, such as distributed micro-cracks. In the literature the higher harmonic generation has been employed to evaluate material thermal degradation [31], fatigue microstructure [30, 32], micro-corrosive defect [33] and the dislocation substructures in metals [34, 35].

The higher harmonics can also be generated due to the contact nonlinearity at the contact-type damage. When guided waves propagate in a localized fatigue crack, the compressive and tensile stress at the damaged medium closes and opens the contact interfaces, respectively. This behaviour alters the stiffness of the structure and generates the higher harmonics. In the literature the contact nonlinearity has been investigated for a number of contact-type damages, such as fatigue crack [36], kissing bond [37, 38], debonding [39, 40] and breathing crack[41].

1.3 Numerical simulation of nonlinear guided waves

In the literature different numerical simulation methods have been proposed to simulate the nonlinear guided waves. For example, Shen and Giurgiutiu [42] proposed an analytical and finite element (FE) method to simulate the nonlinear guided wave propagation induced by a breathing crack. The piezoelectric wafer active sensor was implemented to generate and receive the guided wave signals. Wan *et al*. [43] utilized the analytical and FE method to study the higher harmonics induced by the material nonlinearity in plates. Approximate phase velocity matching condition for the generation of nonlinear signal was investigated using the low frequency primary mode Lamb waves. Hong *et al*. [20] employed the FE method to simulate the nonlinear guided wave in aluminium plates with fatigue cracks. Zhu *et al*. [44] utilized the FE method to study the plastic damage in martensite stainless steels. The nonlinear guided wave due to material and geometric nonlinearities was analyzed by incorporating a nonlinear constitutive relationship to FE models. Yamanako *et al*. [45] proposed a two dimensions (2D) finite difference (FD) method to analysis nonlinear guided wave. The subharmonic generation at closed stress corrosion cracks was successfully reproduced. Shen and Cesnik [46] utilized the local interaction simulation approach (LISA) to simulate the nonlinear guided wave caused by the clapping mechanism of fatigue cracks. Joglekar and Mitra [47] proposed a fast Fourier transform (FFT) based spectral finite element (SFE) model to study the nonlinear guided wave in beams due to the breathing crack. He and Ng [48] proposed a time-domain SFE method, which employed a crack-breathing mechanism to simulate the contact nonlinearity. They investigated the performance of the fundamental symmetric (S_0) and anti-symmetrical (A_0) mode and also the mode conversion in generating the higher harmonics in the breathing crack.

The existing numerical simulation methods have different advantages and disadvantages. The FFT based SFE method is computational efficient in modeling guided wave propagation, but it is a semi-analytical method assuming infinite length of the structure. The FD method can simulate on large scale model under regular grids. However, it is incapable of simulating the guided wave propagation in waveguides if material property changes with geometry [49]. The LISA is efficient and effective in simulating complex geometries but it requires careful discretization to obtain accurate solutions. The major distinction between FE method and SFE method is the use of shape function. Although the FE method is suitable to simulate complex structures, the efficiency of computation is unsatisfied since the shape function is not in a high order. The discretization of the FE elements should be very small to ensure the accuracy of the simulation.

Overall, it is found that most of the simulation concern only the contact nonlinearity or, to a less extent, the material and geometric nonlinearities. Very limited papers [20] considered all the contribution of material, geometric and contact nonlinearities in the second harmonics generation (SHG), especially for beam structures and time-domain SFE method. In this study, time-domain SFE model is proposed to study the SHG in beams with a breathing crack with the consideration of material, geometric and contact nonlinearities. The findings of the study can provide physical insights into the SHG due to the material, geometric and contact nonlinearities. This can further advance the development of using SHG for damage detection.

1.4 Time-domain spectral finite element method

The time-domain SFE has been found to be computationally efficient in the simulation of guided wave propagation and capable of modeling complicated geometric structures. The time-domain SFE method is as flexible as the conventional FE method in modeling different geometries of structures. The computational efficiency is significantly improved by using the high-order approximation polynomials. Gauss-Lobatto-Legendre (GLL) nodes are applied in a higher-order interpolation. GLL integration points are used to simulate guided waves since it turns mass matrix into a diagonal form. The model can efficiently calculate the solution of the dynamic equilibrium using the explicit central difference method.

The time-domain SFE method has been widely investigated by a number of studies with respect to the linear features of guided waves [50] and damage detection [5]. However, there were limited studies focused on using time-domain SFE method in simulating nonlinear guided waves induced by material, geometric nonlinearities, and contact nonlinearities. In this paper, the computationally efficient time-domain SFE method is extended to take into account the effects of the material, geometric and contract nonlinearities on the SHG.

The arrangement of the paper is as follows. The time-domain SFE method for simulating the nonlinear guided waves is proposed in Section 2. The nonlinear guided waves resulted from material, geometric and contact nonlinearities are formulated in this section. The proposed SFE method for simulating material and geometric nonlinearities, and contact nonlinearity are then validated using analytical solutions and three-dimensional (3D) FE simulations in Section 3. Section 4 carries out a series of numerical case studies to investigate the performance of the proposed SFE method in simulating the SHG at fatigue cracks with the consideration of material, geometric and contact nonlinearities. Conclusions are drawn in Section 5.

2 Time-domain Spectral finite element method

The simulation of nonlinear guided waves using time-domain SFE method is presented in this section. The basic SFE formulation is described first in subsection 2.1. Then the modeling of material and geometric nonlinearities, and contact nonlinearities using the SFE method are described in subsections 2.2 and 2.3, respectively.

2.1 Spectral finite element formulation

The dynamic equilibrium of the time-domain SFE method is the same as the conventional FE method, which is defined as [48,52]

$$\mathbf{M}\ddot{\mathbf{U}}+\mathbf{C}\dot{\mathbf{U}}+\mathbf{K}\mathbf{U}=\mathbf{F}(t) \tag{1}$$

where $\mathbf{M}$, $\mathbf{K}$ and $\mathbf{F}(t)$ are global mass matrix, global stiffness matrix and global force vector at time t, respectively. The global damping matrix $\mathbf{C}$ is a function of the global mass matrix denoted by $\mathbf{C}=\eta\mathbf{M}$, where η is the damping coefficient. $\ddot{\mathbf{U}}$, $\dot{\mathbf{U}}$ and $\mathbf{U}$ denote the vector of acceleration, velocity and displacement response, respectively. The elemental mass matrix $\mathbf{M}^e$, elemental stiffness matrix $\mathbf{K}^e$ and elemental force vector $\mathbf{F}^e$ that form the corresponding global terms in Equation (1) are given as [10]

$$\mathbf{M}^e \approx \sum_{i=1}^{n} w_i \mathbf{N}_e(\xi_i)^T \mathbf{r}_e \mathbf{N}_e(\xi_i)\det\left(J(\xi_i)\right) \tag{2}$$

$$\mathbf{K}^e \approx \sum_{i=1}^{n} w_i \mathbf{B}_e(\xi_i)^T \mathbf{E}_e \mathbf{B}_e(\xi_i)\det\left(J(\xi_i)\right) \tag{3}$$

$$\mathbf{F}^e(t) \approx \sum_{i=1}^{n} w_i \mathbf{N}_e(\xi_i)^T \mathbf{f}_e(t) \mathbf{N}_e(\xi_i)\det\left(J(\xi_i)\right) \tag{4}$$

where ξ_i is the local coordinate of the i-th node at the element, $i \in 1,\dots,n$, and n is the number of nodes. $J=\partial x/\partial\xi$ is the Jacobian functions transferring the local coordinate ξ to the global coordinate x. w_i is the weighting function of node i defined as $w_i = 2/\{n(n-1)[L_{n-1}(\xi_i)]^2\}$.

$\mathbf{r}_e = diag\left[\begin{array}{cccc} \rho bh & K_2^M \rho bh^3/12 & \rho bh & K_2^T \rho bh^3/12 \end{array}\right]$ is the mass matrix, where ρ is the density of the material, b is the width and h is the height of the beam. $\mathbf{E}_e$ is the material property matrix and $\mathbf{f}_e(t)$ is the external force vector at time t applied to the element, respectively. Different to the conventional FE method, the SFE method employs the GLL nodes in the element, which results in a more efficient solution than the FE method [48]. The local coordinate ξ_i of the GLL nodes can be determined from the roots of the given equation

$$\left(1-\xi_i^2\right)L'_{n-1}\left(\xi_i\right)=0 \quad \text{for} \quad \xi_i \in [-1,1] \text{ and } i \in 1,\ldots,n \tag{5}$$

where L'_{n-1} denotes the first derivative of (n-1)-th order Legendre polynomial. $\mathbf{N}_e$ is the shape function of the SFE element, which has the matrix form [15]

$$\mathbf{N}_e = \left[N_1(\xi),\ldots,N_n(\xi)\right]\otimes\mathbf{I} \qquad \text{where } N_i(\xi)=\prod_{m=1,m\neq i}^{n}\frac{\xi-\xi_m}{\xi_i-\xi_m} \tag{6}$$

where m is the sequence of the n GLL integration points in the element. $\mathbf{I}$ is an identity matrix with the square size same as the number of the nodal degree of freedom. '$\otimes$' denotes the Kronecker product.

In this paper, the first-order shear deformation theory considering the independent contraction due to Poisson effect is employed to formulate the beam element. The displacement field is defined as [15]

$$\bar{u}(x,y)\approx u(x)-\varphi(x)y \quad \text{and} \quad \bar{v}(x,y)\approx v(x)+\psi(x)y \tag{7}$$

where $u(x)$ is the longitudinal displacement in x axis direction, v is the transverse displacement, φ is the rotation of the cross section and ψ is the independent contraction accounts for the Poisson effect. The Lagrange strain [52] is employed and the strain field in the element is defined as

$$\boldsymbol{\varepsilon}^e = \mathbf{B}^e\mathbf{q}^e = \left(\mathbf{B}_L^e + \mathbf{B}_{NL}^e\right)\mathbf{q}^e \tag{8}$$

where $\mathbf{q}^e = [u^e, \psi^e, v^e, \varphi^e]^T$ and $\mathbf{B}^e$ is strain-displacement operator. $\mathbf{B}_L^e$ and $\mathbf{B}_{NL}^e$ account for the first and second order terms of Lagrange strain and they are defined as

$$\mathbf{B}_L^e = \begin{bmatrix} \frac{\partial}{\partial x} & 0 & 0 & 0 \\ 0 & 1 & 0 & 0 \\ 0 & \frac{\partial}{\partial x} & 0 & 0 \\ 0 & 0 & \frac{\partial}{\partial x} & -1 \\ 0 & 0 & 0 & \frac{\partial}{\partial x} \end{bmatrix} \mathbf{N}^e \quad \text{and} \quad \mathbf{B}_{NL}^e = \frac{1}{2} \begin{bmatrix} \frac{\partial u^e}{\partial x}\frac{\partial}{\partial x} & 0 & \frac{\partial v^e}{\partial x}\frac{\partial}{\partial x} & 0 \\ 0 & \psi^e & 0 & \varphi^e \\ 0 & 0 & 0 & 0 \\ 0 & 0 & 0 & 0 \\ 0 & 0 & 0 & 0 \end{bmatrix} \mathbf{N}^e \tag{9}$$

2.2 Modeling of material and geometric nonlinearities

Considering an isotropic homogeneous solid with purely elastic behavior, the material and geometric nonlinearities can be represented by the constitutive relation between stress and strain using the second order approximation [54] as

$$\sigma_{ij} = \left(Q_{ijkl}^L + 1/2\, Q_{ijklmn}^{NL} \varepsilon_{mn} \right) \varepsilon_{kl} \tag{10}$$

where σ_{ij} is the stress tensor. ε_{mn} and ε_{kl} are the strain tensors. Q_{ijkl}^L is the second order elastic tensors, which can be expressed in a matrix form for two-dimensional plane stress situation as

$$\left\{ Q_{ijkl}^L \right\} = \begin{bmatrix} Q_{1111}^L & Q_{1133}^L & 0 \\ Q_{1133}^L & Q_{3333}^L & 0 \\ 0 & 0 & Q_{3131}^L \end{bmatrix} = \frac{E}{\left(1-\upsilon^2\right)} \begin{bmatrix} 1 & \upsilon & 0 \\ \upsilon & 1 & 0 \\ 0 & 0 & \frac{1-\upsilon}{2} \end{bmatrix} \tag{11}$$

where $\upsilon = 0.5\lambda/(\lambda+\mu)$ is the Poisson's ratio and $E = \mu(3\lambda+2\mu)/(\lambda+\mu)$ is the Young's modulus of the material. λ and μ are the Lamé constants. Q_{ijklmn}^{NL} is the tensor addresses both the material and geometric nonlinearities. If Q_{ijklmn}^{NL} is not considered, Equation (10) can be simplified into the linear situation following the Hooke's Law. The form of Q_{ijklmn}^{NL} is given as [20, 43, 54].

$$Q_{ijklmn}^{NL} = Q_{ijklmn}^L + Q_{ijln}^L \delta_{km} + Q_{jnkl}^L \delta_{im} + Q_{jlmn}^L \delta_{ik} \tag{12}$$

where

$$Q_{ijklmn}^L = \frac{1}{2} A\left(\delta_{ik} I_{jlmn} + \delta_{il} I_{jkmn} + \delta_{jk} I_{ilmn} + \delta_{jl} I_{ikmn} \right) + 2B\left(\delta_{ij} I_{klmn} + \delta_{kl} I_{mnij} + \delta_{mn} I_{ijkl} \right) + 2C \delta_{ij} \delta_{kl} \delta_{mn} \tag{13}$$

In Equation (12) and (13), δ_{ij} and its similar forms with different subscript indexes are the Kronecker delta. I_{ijkl} and its similar forms with different index orders are the fourth order identity tensors.

The material nonlinearity is described by the third order elastic tensor Q_{ijklmn}^{NL}, where the geometric nonlinearity is addressed by the last three terms in Equation (12). The subscript *ij*, *kl*, *mn* = 11, 33, 31 in this paper. The third order elastic tensor Q_{ijklmn}^{NL} is determined by three third order elastic constants *A*, *B* and *C*. Their values can be measured from experiment for the investigated materials. Let $Q_{ijkl} = Q_{ijkl}^{L} + 1/2 Q_{ijklmn}^{NL} \varepsilon_{mn}$, the material property matrix $\mathbf{E}_e$ in Equation (3) is expressed as

$$\mathbf{E}_e = \begin{bmatrix} Q_{1111}bh & Q_{1133}bh & 0 & 0 & 0 \\ Q_{1133}bh & Q_{3333}bh & 0 & 0 & 0 \\ 0 & 0 & Q_{3131}K_1^M bh^3/12 & 0 & 0 \\ 0 & 0 & 0 & Q_{3131}K_1^T bh & 0 \\ 0 & 0 & 0 & 0 & Q_{3333}bh^3/12 \end{bmatrix} \tag{14}$$

where $K_1^M = 1.1$, $K_2^M = 3.1$, $K_1^T = 0.922$ and $K_2^T = 12K_1^T/\pi^2$ are adjustable parameters that calibrate the accuracy of guided wave propagation simulation [9]. Using the material property matrix $\mathbf{E}_e$ in Equation (14), the time-domain SFE method can include the effect of the material nonlinearity in simulating the guided wave propagation.

2.3 Acoustic nonlinearity parameter

For one-dimensional (1D) longitudinal wave propagation, Equation (10) can be simplified as [21, 43]

$$\sigma = \left(E + E_2\varepsilon\right)\varepsilon \tag{15}$$

where σ, ε and E_2 are the stress, strain and the second order Young's modulus accounted for the nonlinearity of the medium [53]. E_2 can be calculated from

$$E_2 = -\frac{1}{2}\left(3E + 2A + 6B + 2C\right) \tag{16}$$

In order to investigate the nonlinearity of the material, the acoustic nonlinearity parameter β is introduced as the ratio of the second order Young's modulus to Young's modulus as [20]

$$\beta = \frac{E_2}{E} = -\frac{1}{2}\left(3 + \frac{2A + 6B + 2C}{E}\right) \tag{17}$$

Equation (17) shows that the acoustic nonlinearity parameter β is a function of the Young's modulus, which accounts for the linear behavior of the medium, and the third order elastic constants *A*, *B* and *C*, which account for the nonlinear behavior of the medium. This shows that the acoustic nonlinearity parameter β quantifies the degree of material nonlinearity of the medium without any defect or plastic deformation. In practice, the relative acoustic nonlinearity parameter β' can be employed as an indicator to study the second order of the medium nonlinearity [55], which is defined as the ratio between the spectral amplitude at the second harmonic frequency (A_2) and the square of the spectral amplitude of the fundamental frequency (A_1) as

$$\beta' = \frac{A_2}{A_1^2} \tag{18}$$

According to the reference [56], the relative acoustic nonlinearity parameter β' is linearly proportion to the nonlinear parameter β and the wave propagation distance if the measured guided wave modes are cumulative. Hence β' also has the following expression

$$\beta' \propto \beta x \tag{19}$$

where x is the distance of propagation. Hence, the relative acoustic nonlinearity parameter β' indicates the nature of the nonlinear property of the wave propagation.

2.4 Modeling of contact nonlinearity

In this paper, the contact nonlinearity induced by a breathing crack in a cracked beam is also simulated by the proposed SFE model. To achieve this, a SFE cracked element is proposed in this section. Considering a cracked beam with length L, width b and height h, the breathing crack with depth d_c is modeled at location L_c of the beam. Figure 1(a) shows the SFE discretization of the beam. The intact part of the beam is modeled using the SFE beam element and the cracked part is modeled by the proposed SFE cracked element. Eight GLL nodes are used by the SFE beam element while two GLL nodes are used in the proposed SFE cracked element. The nodes in the crack element consider three degrees-of-freedom (DoFs) i.e., longitudinal, transverse and rotational DoFs. The length of the crack element is assumed to be very small, i.e. $l \approx 0.001$ mm, in the model. When the proposed cracked element is connected with the SFE beam element, the lateral contraction DoF induced by the longitudinal wave propagation is not considered due to the very small length of the proposed SFE crack element.

[Figure 1. Schematic diagram of a SFE model for simulating a cracked beam, (a) discretization of a cracked beam; (b) two-node SFE crack element when the crack is opened and closed]

The contact nonlinearity due to the breathing phenomenon of the crack is modeled by a contact mechanism indicated in Figure 1(b). The nodal longitudinal displacements u_1 and u_2 at the SFE cracked element are examined to determine the status of the crack at each time step of the simulation:

$$u_1 - u_2 < 0 \text{ when the crack is opened} \tag{20}$$

$$u_1 - u_2 >= 0 \text{ when the crack is closed} \tag{21}$$

Based on the status of the crack, the stiffness matrix $\mathbf{K}_e^c$ of the SFE crack element can be determined. When the crack is opened, the stiffness matrix $\mathbf{K}_e^c$ of the SFE crack element is calculated as [48]

$$\mathbf{K}_e^c = \mathbf{P}\mathbf{G}_c^{-1}\mathbf{P}^T \tag{22}$$

where $\mathbf{P}$ is the spatial transformation matrix as a function of the crack element length l

$$\mathbf{P}^T = \begin{bmatrix} 1 & 0 & 0 & -1 & 0 & 0 \\ 0 & 1 & 0 & 0 & -1 & l \\ 0 & 0 & 1 & 0 & 0 & -1 \end{bmatrix} \tag{23}$$

$\mathbf{G}_c$ is the flexibility matrix for the open crack given as follows

$$\mathbf{G}_c = \begin{pmatrix} g_{11}^c & g_{12}^c & g_{13}^c \\ g_{21}^c & g_{22}^c & g_{23}^c \\ g_{31}^c & g_{32}^c & g_{33}^c \end{pmatrix} \tag{24}$$

with

$$g_{11} = \frac{l}{EA} + I_{g1}, \qquad g_{22} = \left(\frac{\kappa l}{GA} + \frac{l^3}{3EA}\right) + \left(I_{g3} + l_c^2 I_{g4}\right), \qquad g_{33} = \frac{l}{EI} + I_{g4},$$

$$g_{12} = g_{21} = l_c I_{g2}, \quad q_{13} = q_{31} = -I_{g2}, \quad q_{23} = q_{32} = -\frac{l^2}{2EI} - l_c I_{g4} \tag{25}$$

where $\kappa = 10(1+\nu)/(12+11\nu)$ is the shear coefficient for rectangular shape of the beam cross section. I_{g1}, I_{g2}, I_{g3} and I_{g4} are the functions of the crack depth defined as

$$I_{g1} = \frac{2\pi}{Eb}\int_0^\alpha \alpha F_1^2 d\alpha, \quad I_{g2} = \frac{12\pi}{Ebh}\int_0^\alpha \alpha F_1 F_2 d\alpha, \quad I_{g3} = \frac{2\kappa\pi}{Eb}\int_0^\alpha \alpha F_{II}{}^2 d\alpha, \quad I_{g4} = \frac{72\pi}{Ebh^2}\int_0^\alpha \alpha F_2^2 d\alpha \tag{26}$$

where l_c is the crack location in the SFE crack element. $\alpha = d_c/h$. F_1, F_2 and F_{II} are the empirical boundary calibration factors accounted for tension, bending and shear of the surface crack, respectively. According to [57], the factors F_1, F_2 and F_{II} produce less than 0.5% errors for the simulation of the crack with any depth d_c. Their formulations are given as [48]

$$F_1(\alpha) = \sqrt{\frac{2}{\pi\alpha}\tan\left(\frac{\pi\alpha}{2}\right)}\,\frac{0.752 + 2.02\alpha + 0.37\left[1-\sin\left(\frac{\pi\alpha}{2}\right)\right]^3}{\cos\left(\frac{\pi\alpha}{2}\right)} \tag{27}$$

$$F_2(\alpha)=\sqrt{\frac{2}{\pi\alpha}\tan\left(\frac{\pi\alpha}{2}\right)}\frac{0.923+0.199\left[1-\sin\left(\frac{\pi\alpha}{2}\right)\right]^4}{\cos\left(\frac{\pi\alpha}{2}\right)} \tag{28}$$

$$F_{II}(\alpha)=\frac{1.122-0.561\alpha+0.085\alpha^2+0.18\alpha^3}{\sqrt{1-\alpha}} \tag{29}$$

When the crack is closed, the crack element is considered as an intact beam element. The SFE crack element stiffness matrix $\mathbf{K}_e^c$ in Equation (22) becomes

$$\mathbf{K}_e^c=\mathbf{P}\mathbf{G}_e^{-1}\mathbf{P}^T \tag{30}$$

where $\mathbf{G}_e$ is the flexibility matrix for the closed crack and is defined as

$$\mathbf{G}_e=\begin{pmatrix} g_{11}^e & g_{12}^e & g_{13}^e \\ g_{21}^e & g_{22}^e & g_{23}^e \\ g_{31}^e & g_{32}^e & g_{33}^e \end{pmatrix} \tag{31}$$

with

$$g_{11}^e=\frac{l}{EA},\qquad g_{22}^e=\left(\frac{\kappa l}{GA}+\frac{l^3}{3EA}\right),\qquad g_{33}^e=\frac{l}{EI},$$

$$g_{12}^e=g_{21}^e=g_{13}^e=g_{31}^e=0,\qquad g_{23}^e=g_{32}^e=-\frac{l^2}{2EI} \tag{32}$$

3 Model validation

The effectiveness of the proposed model is validated in this section. The validation is conducted in two situations. First, the model of material and geometric nonlinearities is verified similar to the approach in reference [43]. It compares the ratio of the relative nonlinear parameter β' between two different materials calculated using SFE and the analytical approach. After that, the conventional FE simulation is used to verify the contact nonlinearity generated due to the interaction between the guided wave and the breathing crack. The results of validations are presented in the following subsections.

3.1 Validation of material and geometric nonlinearities

The aluminium beams with the two different material properties, e.g., Al 6061-T6 and Al 7075-T651 are considered, where the material properties [43] are shown in Table 1. The beams have the same geometric dimensions, where the length *L*, width *b* and height *h* of the beams are 1 m, 12 mm and 5 mm, respectively. The schematic diagram of the SFE model is indicated in Figure 2(a). The excitation signal is an f_0 = 100 kHz, narrow-band, 16-cycle sinusoidal tone burst modulated by a Hanning window. The S_0 guided wave is excited by applying the in-plane displacement at the left end of the beam, in which the maximal amplitude of the input displacement is 1×10^{-6} m. The displacement response is calculated by the SFE simulation at L_m= 0.5 m and the FFT is then employed to determine the spectral amplitude of the first harmonic (A_1) and the second harmonic (A_2) generated by both material and geometric nonlinearities.

[Table 1. Material properties of Al-6061-T6 and Al-7075-T651] [43]

[Figure 2. Schematic diagram of the SFE beam with (a) material and geometric nonlinearities; and (b) material, geometric and contact nonlinearities]

The spectral amplitudes of the SHG A_2 with propagation distance for Al 6061-T6 and Al 7075-T651 are calculated in Figure 3. It shows that the magnitude of the SHG increases until it reaches the maximum cumulated propagation distance (504 mm for Al 6061-T6), after which it decreases due to dissatisfaction of the cumulative condition, i.e., the non-synchronization of the phase velocity between the harmonics at f_0 =100 kHz and $2f_0$ =200 kHz. It also shows that the spectral amplitude of the SHG A_2 does not increase linearly. In order to use Equation (18) to determine the relative nonlinearity parameter β' effectively, the linear regression analysis is utilized to determine the maximum linear cumulative propagation distance, where the coefficient of determination R^2 is set larger than 0.99 in the analysis [43]. Based on the analysis, the maximum linear cumulative propagation distance is calculated (376 mm for Al 6061-T6) and within this distance the higher harmonics are considered 'cumulated'.

[Figure 3. Spectral amplitude of second harmonic against propagation distance for Al 6061-T6 and Al 7075-T651]

The calculated relative nonlinear parameter β' with propagation distance x and the corresponding linear regression are shown in Figure 4. k is the slope of the line, which is proportional to the nonlinear parameter β'. As shown in Figure 4, the slope k for the material A_l 6061-T6 is larger than that of Al 7075-T651. Also, it is shown that the nonlinear parameter β' increases linearly, which indicates that the SHG of S_0 guided wave is cumulated in this propagation distance. Hence, the ratio of the nonlinear parameter of Al 6061-T6 to Al 7075-T651 is $\beta_{Al6061}/\beta_{Al7075} = k_{Al6061}/k_{Al7075} = 0.0298/0.0267 = 1.116$, which is closed to the analytical result, i.e., 1.12, calculated using Equation (17). This shows that the SFE simulation is able to take into account the material and geometric nonlinearities in the guided wave simulations.

[Figure 4. The relative nonlinear parameter β' calculated from the measured displacement against the wave propagation distance for the S_0 incident guided wave at 100 kHz]

3.2 Validation of contact nonlinearity

This subsection validates the contact nonlinearity of the SFE simulation by comparing the SFE results with those calculated by conventional 3D FE simulations. The material of the beam is Al 6061-T6 and the properties are shown in Table 1. The length L, width b and height h of the beam are 1 m, 6 mm and 12 mm, respectively. The crack is located at L_c = 0.5 m and the crack depth is d_c =3 mm. The excitation signal is an f_0 = 50 kHz, narrow-band, 5-cycle sinusoidal tone burst modulated by a Hanning window [**Error! Reference source not found.**]. The S_0 guided wave is generated by applying the in-plane displacement at the left end of the beam. The displacement response is calculated at the same location as the excitation location. The simulation duration is long enough to cover the incident S_0 guided wave propagates from the excitation location to the right end of the beam, and then reflects back to the left end of the beam (the excitation and measurement location). 100 SFE beam elements are used to model the beam to ensure the convergence of simulation and each of SFE beam element has eight GLL nodes. The damping coefficient η is assumed to be 200 s^{-1}. The time step of the simulation is chosen at 2.5×10^{-8} s.

The conventional 3D FE simulations are carried out using the commercial FE software, ABAQUS v6.12-1, to simulate the wave propagating in the cracked beam. The eight-noded 3D solid brick elements (C3D8I) with the incompatible mode are used to model the cracked beam. The option of second-order accuracy is enabled in the incompatible mode in the simulations. The mesh size of the elements is 0.4mm×0.4mm×0.4mm to ascertain the stability of the FE simulations. The crack is modeled by duplicating the nodes at the crack interfaces [59, 60]. The contact nonlinearity due to the breathing phenomenon is simulated by assigning the 'frictionless hard contact' property to the crack interfaces. The S_0 guided wave is excited by applying the in-plane nodal displacement at the vertical surface of the left beam end. The excitation signal is the same as the SFE simulations. The explicit solver, ABAQUS/Explicit, is used to solve the dynamic problem. The time step is automatically controlled by ABAQUS/Explicit in the simulations.

The simulation results are shown in Figure 5. Figure 5(a) shows the response displacement in time-domain, which is normalized to the peak amplitude of the incident wave. There is good agreement between the results of the SFE and FE simulations. Figure 5(b) shows the FFT of the displacement response. The figure shows that the results of the SFE and FE have the same spectral amplitude of the second harmonic at $2f_0 = 100$ kHz. This demonstrates the accuracy of the proposed SFE method in simulating the nonlinear guided wave induced by the contact nonlinearity at the breathing crack.

[Figure 5. Comparison of SFE and FE simulated results in (a) time-domain; (b) frequency-domain]

3.3 Three-dimensional finite element validation

A material subroutine developed in ABAQUS/Explicit is used to ensure the accuracy of the proposed time-domain SFE model. The subroutine applies Murnaghan's energy function [61] in order to model the S_o guided wave in Aluminium beams. The material nonlinearity in ABAQUS VUMAT is formulated by a set of constitutive equation. The deformation gradient **F** links the reference configuration **X** (material) to the current configuration **x** (spatial) and is written as [62]

$$\mathbf{F} = \frac{\partial \mathbf{x}}{\partial \mathbf{X}} \tag{33}$$

The Green-Lagrange strain tensor is employed in this study and is defined as

$$\mathbf{E} = \frac{1}{2}(\mathbf{C} - \mathbf{I}) \tag{34}$$

where **C** is the right Cauchy-Green deformation tensor and **I** is the identity tensor. **C** is related to the deformation gradient **F**

$$\mathbf{C} = \mathbf{F}^{\mathrm{T}}\mathbf{F} = \mathbf{U}^{2} \tag{35}$$

where **U** is the right stretch tensor.

The nonlinear strain energy function of Murnaghan is given as

$$W(\mathbf{E}) = \frac{1}{2}(\lambda + 2\mu)i_1^2 - 2\mu i_2 + \frac{1}{3}(B + C)i_1^2 - 2Ci_1 i_2 + Ai_3 \tag{36}$$

where λ and μ are the Lamé elastic constants; A, B and C are the third order elastic constants. $i_1 = tr\mathbf{E}$, $i_2 = \frac{1}{2}[i_1^2 - tr(\mathbf{E})^2]$, $i_3 = det\mathbf{E}$, respectively.

User material subroutine VUMAT in ABAQUS/Explicit can define the mechanical constitutive behaviour for material nonlinearity in modeling guided wave. The Green-Naghdi rate of the Cauchy stress tensor is utilized in VUMAT.

$$\hat{\boldsymbol{\sigma}} = \mathbf{R}^{\mathrm{T}}\boldsymbol{\sigma}\mathbf{R} \tag{37}$$

where **R** is rotation tensor, and R is a proper orthogonal tensor, i.e., $\mathbf{R}^{-1} = \mathbf{R}^{\mathrm{T}}$. The terms **F**, **U** and **R** are related as follow

$$\mathbf{F} = \mathbf{R}\mathbf{U} \tag{38}$$

The relationship of the second Piola-Kirchhoff (PK2) stress **T** and the strain energy function in Equation (36) is given by

$$\mathbf{T} = \frac{\partial W(E)}{\partial E} \tag{39}$$

The Cauchy stress and the PK2 stress are interrelated and written as

$$\hat{\boldsymbol{\sigma}} = \mathrm{J}_1{}^{-1}\mathbf{F}\mathbf{T}\mathbf{F}^{\mathrm{T}} = \mathrm{J}_1{}^{-1}\mathbf{F}\frac{\partial W(\mathbf{E})}{\partial \mathbf{E}}\mathbf{F}^{\mathrm{T}} \tag{40}$$

where $\mathrm{J}_1 = \det(\mathbf{F})$.

By substituting Equations (38)-(40) into Equation (37)

$$\hat{\boldsymbol{\sigma}} = \mathrm{J}_1{}^{-1}\mathbf{R}^{\mathrm{T}}\mathbf{F}\mathbf{T}\mathbf{F}^{\mathrm{T}}\mathbf{R} = \mathrm{J}_1{}^{-1}\mathbf{R}^{\mathrm{T}}\mathbf{R}\mathbf{U}\mathbf{T}\mathbf{U}^{\mathrm{T}}\mathbf{R}^{\mathrm{T}}\mathbf{R} = \mathrm{J}_1{}^{-1}\mathbf{U}\frac{\partial W(\mathbf{E})}{\partial \mathbf{E}}\mathbf{U}^{\mathrm{T}} \tag{41}$$

Depending on the values of **F** and **U** provided in the user subroutine at the end of previous time step (t), the updated stress equation at the end of an integration step $(t + \Delta t)$ is stored in stressNew(i).

3.4 *Comparison of the proposed SFE model and FE model using subroutine*

The material properties of 6061-T6 aluminium beam are used for both the SFE and FE models. The length *L*, width *b* and height *h* of the beam are 1m, 5mm and 12mm, respectively. A 3D eight-node linear brick with reduced integration (C3D8R) are used to model the beam. The dimension of an element is 0.4×0.4×0.4mm^3. The excitation signal is a f_o = 100kHz, narrow-band, 12 cycles sinusoidal tone burst modulated by a Hanning window. The excitation signal of the S_o guided wave is applied to the in-plane nodal displacement on the vertical surface of the left end beam end.

For the SFE model, 8 GLL nodes with 0.01m long in each SFE element are used. The time step is selected at 5×10^{-8} s to ensure the simulation to be converged. The S_o guided wave is loaded by applying the in-plane displacement at the left end of the beam. The excitation signal is the same as the FE model with VUMAT subroutine. The displacement response for both of the SFE simulation and the FE model are measured at L_m = 0.5m.

[Figure 6 Comparison of SFE and FE simulations for linear and nonlinear perspective in terms of (a) time-domain; (b) frequency domain, and (c) the triggered signal in frequency domain]

The solid lines represent the signal in nonlinear response while the dashed lines refer to linear response. The SFE signals are shown in red color and the FE signals are labeled in blue color. The amplitude of each time-domain displacement response in Figure 6(a) is normalized. Figure 6(b) shows the corresponding signals in frequency domain. It is shown that the linear signals of both the SFE and FE models does not carry any second harmonic information. After implementing material nonlinearity, both the SFE and FE simulations generate second harmonic at $2f_o = 200$kHz with similar second harmonic peak.

4 Numerical case studies and discussions

A series of numerical case studies are carried out in this section to investigate the performance of the proposed SFE model. The performance of the SFE model in simulating the material and geometric nonlinearities is studied first, which investigates the influences of different numbers of cycles and amplitudes of the excitation signal on the SHG in Section 4.1. After that, the contribution of the material and geometric nonlinearities, and the contact nonlinearity to the SHG is studied in Section 4.2. The beam with length L= 1 m, depth d=5 mm and width b=12 mm is simulated in this study and the material is assumed to be Al 6061-T6 and the material properties are shown in Table 1.

4.1 Second harmonic generation (SHG) due to material and geometric nonlinearities

In this part, the influence of the geometric and material nonlinearities on the SHG is studied in Section 4.1.1. The influences of different numbers of cycles and the amplitudes of excitation signal on the SHG due to geometric and material nonlinearities are studied in Sections 4.1.2 and 4.1.3, respectively.

4.1.1 Influence of material and geometric nonlinearities

This section studies the influence of the material and geometric nonlinearities on the SHG. The excitation signal is a 100 kHz, narrow-band, 16-cycle sinusoidal tone burst modulated by a Hanning window. The S_0 guided wave is generated by applying the in-plane displacement with the maximum amplitude of 1×10^{-6} m to the left end of the beam, and the displacement response is measured at L_m= 0.5 m. Based on Equation (12), the first term on the right hand side of the equation accounts for the material nonlinearity and the other three terms address the geometric nonlinearity. This section considers three different situations: 1) linear, 2) only geometrically nonlinear, and 3) nonlinear with both material and geometric nonlinearities. In the linear situation, the term Q_{ijklmn}^{NL} in Equation (10) is not considered in the simulation. For the geometrically nonlinear situation, the first term of right hand side of Equation (12), i.e. Q_{ijklmn}^{L}, is neglected. For the nonlinear situation that considers both material and geometric nonlinearities, all the terms at the right hand side of Equation (12) are considered in the simulations. The calculated time-domain displacement responses of these three situations are shown in Figure 7.

[Figure 7. The calculated time-domain displacement response at L_m= 0.5 m for linear situation, and situations consider only geometric nonlinearity, and both material and geometric nonlinearities in the SFE simulation]

From the time-domain signal shown in Figure 7, the difference between the nonlinear situations and the linear situation is hardly distinguished. Figure 8 shows the FFT of the calculated displacement responses at L_m= 0.5 m for the three aforementioned situations. Compared with the time-domain signal, the SHG in the nonlinear situation (with geometric and material nonlinearities) is clearly observed. Furthermore, the results show that the spectral amplitude of the SHG for the situation considering both material and geometric nonlinearities is about 10 times greater than that of the situation considering only the geometric nonlinearity. This demonstrates that the SHG is mainly due to the material nonlinearity.

[Figure 8. FFT of the calculated displacement responses at L_m= 0.5 m for linear situation, and situations consider only geometric nonlinearity, and both material and geometric nonlinearities in the SFE simulation]

4.1.2 Influence of the numbers of cycles of the excitation signal

The influence of the numbers of cycles of the excitation signal on the SHG due to material and geometric nonlinearities is studied in this section. The excitation signals with 8, 12, 16 and 20 cycles are considered in this study. The signal is a 100 kHz narrow-band sinusoidal tone burst modulated by a Hanning window. The S_0 guided wave is excited by applying the in-plane displacement with the maximal amplitude 1×10^{-6} m at the left end of the beam. The displacement responses are measured at L_m = 0.5 m. The FFT of the displacement responses for the cases considering different numbers of cycles of the excitation signals are shown in Figure 9. The results show that the bandwidth of the fundamental and second harmonic become wider for excitation signal with less numbers of cycles and the amplitude of the SHG increases with the number of cycles.

[Figure 9. FFT of the calculated displacement responses at L_m= 0.5 m for different excitation cycles]

Figure 10 shows the SHG amplitude versus the fundamental amplitude for different numbers of cycles of the excitation signal. Analytically, because the relative nonlinear parameter β' is a constant within the cumulated wave propagation distance x as shown in Equation (19), the ratio of the SHG amplitude to the square of the fundamental harmonic is also a constant from Equation (18).

Therefore, the result is a straight line in Figure 10. There are good agreements between the analytical results and the SFE simulated results for different numbers of cycles. Overall, it is found that the magnitude of the SHG induced due to the material and geometric nonlinearities increases with the numbers of cycles of the excitation signal.

[Figure 10. The second harmonic amplitude versus the fundamental amplitude for varying number of cycles of the excitation signal (solid line: analytical results; markers: SFE simulation results)]

4.1.3 Influence of the amplitude of the excitation signal

The influence of the amplitude of the excitation signal on the SHG due to geometric and material nonlinearities is studied in this section. The excitation signal applied at the left end of the beam is a 100 kHz narrow-band 16-cycle sinusoidal tone burst modulated by a Hanning window. Eight different amplitudes of the excitation signal are considered and magnitude increases from 1×10^{-6} m to 8×10^{-6} m with the step of 1×10^{-6} m. The displacement response is calculated at $L_m = 0.5$ m and the measured time duration is the same as that in Subsection 4.1.2. The amplitudes of the fundamental harmonic and SHG are extracted from the FFT of displacement responses. Figure 11 shows the SHG amplitude versus the fundamental amplitude for different excitation amplitudes, in which the asterisks denote the numerical results. The results in Figure 11 show that there is good agreement between results of SFE and the analytical results obtained from Equation(18). It is found that the SHG amplitude increases with the excitation amplitude.

[Figure 11. The second harmonic amplitude versus the fundamental amplitude for varying excitation amplitude (solid line: analytical results; markers: SFE simulation results)]

4.2 Contribution of material and geometric nonlinearities, and contact nonlinearity in second harmonic generation (SHG)

The contribution of the material and geometric nonlinearities, and contact nonlinearity in the SHG is studied in this subsection. The excitation signal is a 100 kHz, narrow-band, 5-cycle sinusoidal tone burst modulated by a Hanning window. The S_0 guided wave is excited by applying the in-plane displacement with the maximum amplitude of 1×10^{-6} m to the left end of the beam, and the displacement response is measured at L_m =0 m. The breathing crack is located at $L_c = 0.5$ m. Because the crack location $L_c < 0.504$ m, it allows a simulation of the cumulated SHG from material and geometric nonlinearities as discussed in Section 3.1.

Two situations are considered: 1) only contact nonlinearity and 2) both material and geometric nonlinearities, and contact nonlinearity in the SFE simulation. The spectral amplitudes of the SHG as a function of normalized crack depth (d_c/h) are investigated for both situations. The short-time Fourier transformed (STFT) is used to obtain the spectral amplitude of the SHG induced by the crack. Figure 12(a) shows an example of the spectrogram obtained from STFT, and the corresponding time-domain displacement is shown in Figure 12(b). The data is obtained from a beam model with a crack having d_c=2.5 mm. It should be noted that the amplitude of second harmonic guided wave reflected from the breathing crack is labelled as A_2 in Figure 12(a), which is normalized by amplitude of the fundamental harmonic A_1 of the incident guided wave.

[Figure 12. (a) Spectrogram obtained by STFT and (b) the corresponding time-domain displacement response for a beam model with a crack having d_c =2.5 mm and L_c = 0.5 m]

Figure 13 shows the ratio of the SHG amplitude of the wave reflected from the crack (A_2) to the fundamental harmonic amplitude of the incident wave (A_1) as a function of normalized crack depth to beam depth ratio (d_c/h). The results show that the amplitudes of the SHG calculated by the SFE model with the effect of both material and geometric nonlinearities, and contact nonlinearity are in general greater than the results calculated by the SFE model considering only the contact nonlinearity. In the case when the crack size is small, the SHG amplitude is mainly contributed by the contact nonlinearity. This can be explained by the fact that the amplitude of the wave reflected from the small size of the crack is small. Figure 11 shows that the contribution to the SHG amplitude by the material nonlinearity is linear proportional to the wave amplitude. As the amplitude of the reflected wave is small, the material nonlinearity has only a very limited contribution to the SHG. In the case when the crack size is large, although the contribution of the material nonlinearity to the SHG is larger (because the amplitude of the reflected wave is larger), the SHG amplitude is still mainly contributed by the contact nonlinearity. The largest difference of the ratio of the SHG amplitude of the wave reflected from the crack to the fundamental harmonic amplitude of the incident wave is less than 3%.

[Figure 13. Normalized second harmonic amplitude of the displacement responses as a function of normalized crack depth (d_c/h)]

4.3 Determination of breathing crack location using second harmonic generation (SHG)

This section demonstrates the use of the SHG to determine the location of the breathing crack in the beam. In the numerical case studies, the SHG due to the effect of material and geometric nonlinearities, and contact nonlinearity are considered to simulate a practical situation. Since the proposed method relies on the SHG, which can be extracted at the second harmonic frequency, the proposed method can determine the existence and the location of the crack without using the reference data. This means that it is feasible to be used as a reference-free damage detection method.

When the incident wave is excited, it propagates from the actuator to the breathing crack. The SHG from the contact nonlinearity is generates when incident wave interacts with the breathing crack. The generated second harmonic wave then propagates and then reaches the sensor. First of all, the appearance of the second harmonic wave in the time-frequency spectrum (spectrogram) can indicate the existence of the breathing crack. The arrival time and the group velocity of the second harmonic wave can be determined at the second harmonic frequency from the spectrogram and from the material properties of the beam, respectively. Thus, the crack location (L_c) of the crack can be calculated by

$$L_c = \left[\frac{c_g(f_c)c_g(2f_c)}{c_g(f_c)+c_g(2f_c)} \right] \Delta t \tag{42}$$

where $c_g(f_c)$ and $c_g(2f_c)$ are the group velocity of the incident and reflected guided wave at the excitation frequency (f_c) and second harmonic frequency ($2f_c$), respectively. $\Delta t = t_{2f_c} - t_{f_c}$ is the time difference between the arrival time of incident wave at the excitation frequency (t_{f_c}) and the arrival time of the scattered wave at second harmonic frequency t_{2f_c}. Using Figure 12 as an example, t_{f_c} and t_{2f_c} are the arrival time of the peak amplitude for the incident wave at the excitation frequency A_1 and scattered wave from the breathing crack at the second harmonic frequency A_2, respectively.

A beam made by Al 6061-T6 with length L= 1 m, depth d=5 mm and width b=12 mm is considered in this section. The material properties of the beam are show in Table 1. The S_0 guided wave is used as the incident wave in the damage detection. The S_0 guided wave is excited at the left end of the beam using the in-plane displacement with maximum amplitude of 1×10^{-6} m. The excitation signal is a 100 kHz, narrow-band, 5-cycle sinusoidal tone burst modulated by a Hanning window, which is the same as Section 4.2. The group velocity dispersion curve of the beam is shown in Figure 14. The group velocity at the excitation frequency (100 kHz) and second harmonic frequency (200 kHz) are $c_g(f_c) = 4848.5$ m/s and $c_g(2f_c) = 4585.1$ m/s, respectively. Since pulse-echo approach is used to collect the guided wave for the damage detection purpose, the measurement location is assumed to be the same as the excitation location, i.e. L_m = 0 m. To take into account the effect of the measurement noise, it is assumed that the measured time-domain guided wave signals contain 5% root mean square (RMS) white noise.

[Figure 14. Group velocity dispersion curve for AI 6061-T6 beam]

In the numerical case studies, there are three damage cases and they consider the beam having a breathing crack at different locations and different crack depths. A summary of the damage cases is shown in Table 2. Case 1 considers the breathing crack is located at L_c = 0.8 m and the normalized crack depth ratio is 0.4. Case 2 considers the breathing crack with the same normalized crack depth ratio but the crack is located at L_c = 0.92 m, which is closer to the beam end. Case 3 considers the most challenging situation, in which the normalized crack depth ratio is 0.2. The crack is located very close to the beam end at L_c = 0.95 m.

Figure 15 shows the measured signal in each damage case. For Case 1, the first wave package is the incident S_0 guided wave. The second wave package is the scattered wave from the crack and the last wave package is the reflected incident wave from the beam end. For Case 2, since the crack is closer to the beam end, part of the scattered wave is mixed with the boundary reflection. For Case 3, the scattered wave is completely mixed with the reflection incident wave from the beam end. Without the reference data, it is very difficult for the linear guided wave based damage detection methods to detect the crack. Figure 16 shows the corresponding spectrogram of the measured signal for each damage case, which provides the time-frequency information of the measured wave signal. As shown in Figure 16, the second harmonic wave can be extracted at the second harmonic frequency. In each damage case, the arrival time of the scattered wave at second harmonic frequency t_{2f_c} and the arrival time of the incident wave at excitation frequency t_{f_c} can be determined from the spectrogram. Therefore, Δt can be calculated and the crack location L_c can be estimated using Equation (42). The predicted crack location and the percentage error are shown in the fourth and fifth column of Table 2. Overall, the all predicted crack locations are very close to the true crack location and the maximum percentage error is 0.95%.

[Figure 15. Measured time domain signal for a) Case 1, b) Case 2 and c) Case 3]

[Figure 16. Spectrogram of the measured signals for a) Case 1, b) Case 2 and c) Case 3]

[Table 2. Summary of damage cases]

5 Conclusions

This study has proposed a time-domain SFE modeling of SHG of nonlinear guided wave in beam structures, which takes into account material and geometric nonlinearities, and contact nonlinearity. Specifically, the material and the geometric nonlinearities have been modeled by adapting the constitutive relation between strain and stress using a second order approximation, and the contact nonlinearity resulted from a breathing crack has been simulated by a bilinear SFE crack model. The time-domain SFE simulations of the SHG due to material and geometric nonlinearities, and contact nonlinearity have been validated using analytical results and 3D FE simulations, respectively. The results show that the time-domain SFE method is able to provide an accurate prediction in the SHG.

A series of numerical case studies have been carried out to investigate the influence of the material and geometric nonlinearities and contact nonlinearity on the SHG using the proposed SFE model. The numerical case studies have considered the SHG due to the material and geometric nonlinearities. The results have shown that the material nonlinearity in the contribution to the SHG is much greater than geometric nonlinearity. In addition, the amplitude of the SHG increases with the number of cycles and amplitude of the excitation signal. The numerical case studies have also investigated the amplitude of the SHG at a breathing crack, in which the time-domain SFE model takes into account both material and geometric nonlinearities and contact nonlinearity. The spectral amplitude of the SHG has been studied as a function of the normalized crack depth. The results have shown that the contribution of the material and geometric nonlinearities to the SHG is generally smaller than the contact nonlinearity. It has also shown that as the crack size becomes smaller, the SHG due to the material and geometric nonlinearities become smaller. In Figure 13, the material and geometric nonlinearities contributed a very little effect on the SHG, and most of the response came from contact nonlinearity. The material and geometric nonlinearities can be potentially ignored in the practice of damage identification. In addition, a series of numerical case studies have been presented to show that the second harmonic wave can be used to accurately determine the crack location without using the reference data. Overall, the numerical case studies have gained insights into the SHG due to the material and geometric nonlinearities and contact nonlinearity. The findings of this study could further advance the development of damage detection using SHG of nonlinear guided wave.

Acknowledgement

This work was supported by the Australian Research Council (ARC) under Grant Numbers DP160102233. The support is greatly appreciated.

References

1. T.N. Tallman, S. Gungor, K.W. Wang, C.E. Bakis. (2014). Damage detection and conductivity evolution in carbon nanofiber epoxy via electrical impedance tomography. *Smart Mater. Struct.* **23**(4) (2014) 045034.
2. M. Rucka, W. Witkowski, J. Chróscielewski. K. Wilde. Damage Detection of a T-Shaped Panel by Wave Propagation Analysis in the Plane Stress. *Archives Civil Eng.* **58** (2012) 3-24.
3. W.M. Ostachowicz. Damage detection of structures using spectral finite element method. *Comp. & Struct.* **86**(3-5) (2008) 454-462.
4. H.F. Lam, Y. Tao. Statistical detection of multiple cracks on thin plates utilizing dynamic response. *Eng. Struct.* **32**(10) (2010) 3145-3152.

5. Z. Zhang, M. He, A. Liu, H.K. Singh, K.R. Ramakrishnan, D. Hui, K. Shankar, E.V. Morozov. Vibration-based assessment of delaminations in FRP composite plate. *Composite Part B. Eng.* **144** (2018) 254-266.
6. J. Pan, Z. Zhang, J. Wu, K.R. Ramakrishnan, H.K. Singh. A novel method of vibration modes selection for improving accuracy of frequency-based damage detection. *Composite Part B. Eng* **159** (2019) 437-446.
7. W. Fan, P. Qiao. Vibration-based damage identification methods: a review and comparative study. *Struct. Health Monitor*. **10**(1) (2011) 83-111.
8. P. Aryan, A. Kotousov, C.T. Ng, B. Cazzolato. A model-based method for damage detection with guided waves. *Struct. Contr. Health Monit.* **24**(3) *(*2017) e1884.
9. M. Rucka. Experimental and numerical studies of guided wave damage detection in bars with structural discontinuities. *Archive Applied Mech.* **80**(12) (2010) 1371-1390.
10. C. Yeung, C.T. Ng. Time-domain spectral finite element method for analysis of torsional guided waves scattering and mode conversion by cracks in pipes. *Mech Syst. Sig. Process.* **128** (2019) 305-317.
11. Y.K. An, H. Sohn. Instantaneous crack detection under varying temperature and static loading conditions. *Struct. Contr. Health Monit.* **17**(7) (2010) 730-741.
12. C.T. Ng. On accuracy of analytical modeling of Lamb wave scattering at delaminations in multilayered isotropic plates. *Int. J. Struct. Stab. Dyn.* **15**(8) (2015) 1540010.
13. Y. Yang, C.T. Ng, A. Kotousov. Bolted joint integrity monitoring with second harmonic generated by guided waves. *Struct. Health Monitor*. **18**(1) (2019) 193-204.
14. C. Yang, L. Ye, Z Su, M. Bannister. Some aspects of numerical simulation for Lamb wave propagation in composite laminates. Composite structures, **75**(1-4) (2006) 267-275.
15. S. He, C.T. Ng. A probabilistic approach for quantitative identification of multiple delaminations in laminated composite beams using guided waves. *Eng. Struct.* **127** (2016) 602-614.
16. P. Aryan, A. Kotousov, C.T. Ng, S. Wildy. Reconstruction of baseline time-trace under changing environmental and operational conditions. *Smart Mater. Struct.* **25**(3) (2016) 035018.
17. O. Putkis, A.J. Croxford. Continuous baseline growth and monitoring for guided wave SHM. *Smart Mater. Struct.* **22**(5) (2013) 055029.
18. M. Mohabuth, A. Kotousov, C.T. Ng, L.R.F. Rose. Implication of changing loading conditions on structural health monitoring utilizing guided wave. *Smart Mater. Struct.* **27** (2018) 025003.
19. Y. Yang, C.T. Ng, Kotousov K. Influence of crack opening and incident wave angle on second harmonic generation of Lamb waves. *Smart Mater. Struct.* **27** (2019) 055013.
20. M. Hong, Z. Su, Q. Wang, L. Cheng, X. Qing. Modeling nonlinearities of ultrasonic waves for fatigue damage characterization: Theory, simulation, and experimental validation. *Ultrasonics* **54**(3) (2014) 770-778.
21. K. H. Matlack, J. Y. Kim, L. J. Jacobs, J. Qu. Experimental characterization of efficient second harmonic generation of Lamb wave modes in a nonlinear elastic isotropic plate. *J. Appl. Phys.* **109**(1) (2011) 014905.
22. Y. Yang, C.T. Ng, A. Kotousov. Second harmonic generation of guided wave at crack-induced debonding in FRP-strengthened metallic plate. *Int. J. Struct. Stab. Dyn.* **19**(1) (2019) 1940006.
23. I. Solodov, J. Wackerl, K. Pfleiderer, G. Busse. Nonlinear self-modulation and subharmonic acoustic spectroscopy for damage detection and location. *Appl. Phys. Lett.* **84**(26) (2004) 5386-5388.
24. C.S. Park, J.W. Kim, S. Cho, D.C. Seo. A high resolution approach for nonlinear sub-harmonic imaging. *NDT & E International* **79** (2016) 114-122.
25. J. Kober and Z. Prevorovsky. A high resolution approach for nonlinear sub-harmonic imaging. *NDT & E International* **79** (2016) 114-122.
26. H. Sohn, H.J. Lim, M.P. DeSimio, K. Brown, M. Derriso. Nonlinear ultrasonic wave modulation for online fatigue crack detection. *J. Sound Vib.* **333**(5) (2014) 1473-1484.
27. J. Herrmann, J. Y. Kim, L. J. Jacobs, J. Qu, J. W. Littles and M. F. Savage. Assessment of material damage in a nickel-base superalloy using nonlinear Rayleigh surface waves. *J. Appl. Phys.* **99**(12) (2006) 124913.
28. M. Mohabuth, A. Khanna, J. Hughes, J. Vidler, A. Kotousov, C. T. Ng. On the determination of the third-order elastic constants of homogeneous isotropic materials utilizing Rayleigh waves. *Ultrasonics* **96** (2019) 96-103.
29. Y. Liu, V. K. Chillara and C. J. Lissenden. On selection of primary modes for generation of strong internally resonant second harmonics in plate. *J. Sound Vib.* **332**(19) (2013) 4517-4528.
30. C. Lissenden, Y. Liu, G. Choi and X. Yao. Effect of localized microstructure evolution on higher

harmonic generation of guided waves. *J. Nondestr. Eval.* **33**(2) (2014) 178-186.
31. Y. Xiang, M. Deng, F. Z. Xuan and C.-J. Liu. Experimental study of thermal degradation in ferritic Cr–Ni alloy steel plates using nonlinear Lamb waves. *Ndt & E International* **44**(8) (2011) 768-774.
32. M. Deng and J. Pei. Assessment of accumulated fatigue damage in solid plates using nonlinear Lamb wave approach. *Appl. Phys. Lett.* **90**(12) (2007) 121902.
33. W. Li and Y. Cho. Combination of nonlinear ultrasonics and guided wave tomography for imaging the micro-defects. *Ultrasonics* **65** (2016) 87-95.
34. C. Pruell, J. Y. Kim, J. Qu and L. J. Jacobs. A nonlinear-guided wave technique for evaluating plasticity-driven material damage in a metal plate. *NDT & E International* **42**(3) (2009) 199-203.
35. Y. Xiang, M. Deng and F.-Z. Xuan. Creep damage characterization using nonlinear ultrasonic guided wave method: A mesoscale model. *J. Appl. Phys.* **115**(4) (2014) 044914.
36. K. Dziedziech, L. Pieczonka, P. Kijanka and W. J. Staszewski. Enhanced nonlinear crack-wave interactions for structural damage detection based on guided ultrasonic waves. Contr. Health Monit. **23**(8) (2016) 1108-1120.
37. D. Yan, S. A. Neild and B. W. Drinkwater. Modelling and measurement of the nonlinear behaviour of kissing bonds in adhesive joints. *NDT & E International* **47** (2012) 18-25.
38. M. F. Najib and A. S. Nobari. Kissing bond detection in structural adhesive joints using nonlinear dynamic characteristics. *Int. J. Adhes.* **63** (2015) 46-56.
39. H. Mohseni, C. T. Ng. Higher harmonic generation of Rayleigh wave at debondings in FRP-retrofitted concrete structures. *Smart Mater. Struct*. **27** (2018) 105038.
40. C. T. Ng, H. Mohseni, H. F. Lam. Debonding detection in CFRP-retrofitted reinforced concrete structures using nonlinear Rayleigh wave. *Mech. Syst. Sig. Process*. **125** (2019) 245-256.
41. D. Broda, W. J. Staszewski, A. Martowicz, T. Uhl and V. V. Silberschmidt. Modelling of nonlinear crack–wave interactions for damage detection based on ultrasound—A review. *J. Sound Vib.* **333**(4) (2014) 1097-1118.
42. Y. Shen and V. Giurgiutiu. Predictive modeling of nonlinear wave propagation for structural health monitoring with piezoelectric wafer active sensors. *J. Intell. Mater. Syst. Struct.* **25**(4) (2014) 506-520.
43. X. Wan, P. Tse, G. Xu, T. Tao and Q. Zhang. Analytical and numerical studies of approximate phase velocity matching based nonlinear S0 mode Lamb waves for the detection of evenly distributed microstructural changes. *Smart Mater. Struct.* **25**(4) (2016) 045023.
44. W. Zhu, M. Deng, Y. Xiang, F. Z. Xuan, C. Liu and Y. N. Wang. Modeling of ultrasonic nonlinearities for dislocation evolution in plastically deformed materials: Simulation and experimental validation. *Ultrasonics* **68** (2016) 134-141.
45. K. Yamanaka, Y. Ohara, M. Oguma and Y. Shintaku. Two-dimensional analysis of subharmonic ultrasound generation at closed cracks by damped double nodes. *Applied Physics Express* **4** (2011) 076601.
46. Y. Shen, C. E. S. Cesnik. Modeling of nonlinear interactions between guided waves and fatigue cracks using local interaction simulation approach. *Ultrasonics* **74** (2017) 106-123.
47. D. Joglekar, M. Mitra. Analysis of nonlinear frequency mixing in 1D waveguides with a breathing crack using the spectral finite element method. *Smart Mater. Struct.* **24**(11) (2015) 115004.
48. S. He, C.T. Ng. Modelling and analysis of nonlinear guided waves interaction at a breathing crack using time-domain spectral finite element method. *Smart Mater. Struct*. **26**(8) (2017) 085002.
49. F. Xu, Y. Zhang, W. Hong, K. Wu, T. J. Cui. Finite-difference frequency-domain algorithm for modeling guided-wave properties of substrate integrated waveguide. *IEEE Transactions on Microwave Theory and Techniques* **51**(11) (2003) 2221-2227.
50. A. Żak, M. Krawczuk. Assessment of rod behaviour theories used in spectral finite element modelling. *J. Sound Vibrat.* **329**(11) (2010) 2099-2113.
51. P. Kudela, M. Krawczuk, W. Ostachowicz. Wave propagation modelling in 1D structures using spectral finite elements. *J. Sound Vib.* **300**(1-2) (2007) 88-100.
52. P. Kudela, W. Ostachowicz. A multilayer delaminated composite beam and plate elements: reflections of Lamb waves at delamination. *Mechanics of Advanced Materials and Structures* **16**(3) (2009) 174-187.
53. C. Nucera, F. L. d. Scalea. Modeling. of nonlinear guided waves and applications to structural health monitoring. *J. Comput. Civ. Eng.* **29**(4) (2014) B4014001.
54. A. Norris. Finite-amplitude waves in solids. *Nonlinear acoustics* **9** (1998) 263-277.
55. S. Liu, S. Best, S. A. Neild, A. J. Croxford. Z. Zhou. Measuring bulk material nonlinearity using harmonic generation. *NDT & E International* **48** (2012) 46-53.

56. C. Bermes, J. Y. Kim, J. Qu, L. J. Jacobs. Nonlinear Lamb waves for the detection of material nonlinearity. *Mech. Syst. Sig. Process.* **22**(3) (2008) 638-646.
57. H. Tada, P. C. Paris, G. R. Irwin, H. Tada. The analysis of cracks handbook. *New York: ASME Press* 3rd edition (2000).
58. Y. Yang, C. T. Ng, A. Kotousov. Second-order harmonic generation of Lamb wave in prestressed plates. *J Sound Vib*. 460 (2019) 114903.
59. G. T. Pudipeddi, C. T. Ng, A. Kotousov. Mode conversion and scattering of Lamb waves at delaminations in composite laminates. *J Aerospace Eng. ASCE*. **32**(5) (2019) 0401967.
60. H. Mohseni, C. T. Ng. Rayleigh wave propagation and scattering characteristics at debondings in fibre-reinforced polymer-retrofitted concrete structures. *Struct. Health Monitor*. **18**(1) (2019) 303-317.
61. F.D Murnaghan. Finite deformations of an elastic solid. *Am. J. Math.* **59**(2) (1937) 235-260.
62. Y. Yang, C. T. Ng, M. Mohabuth, A. Kotousov. Finite element prediction of acoustoelastic effect associated with Lamb wave propagation in pre-stressed plates. *Smart Mater. Struct*. **28** (2019) 095007.

Tables

Table 1. Material properties of Al-6061-T6 and Al-7075-T651 [41]

Material	ρ (kg m^{-3})	λ (GPa)	μ (GPa)	A (GPa)	B (GPa)	C (GPa)
Al-6061-T6	2704	67.6	25.9	-416	-131	-150.5
Al-7075-T651	2810	70.3	26.96	-351.2	-149.4	-102.8

Table 2. Summary of damage cases

Case	Actual		Predicted	Percentage error
	Crack depth d_c (m)	Crack location L_c (m)	Crack location (m)	
Case 1	0.002	0.8	0.7924	0.95%
Case 2	0.002	0.92	0.9191	0.10%
Case 3	0.001	0.95	0.9426	0.78%

Figures

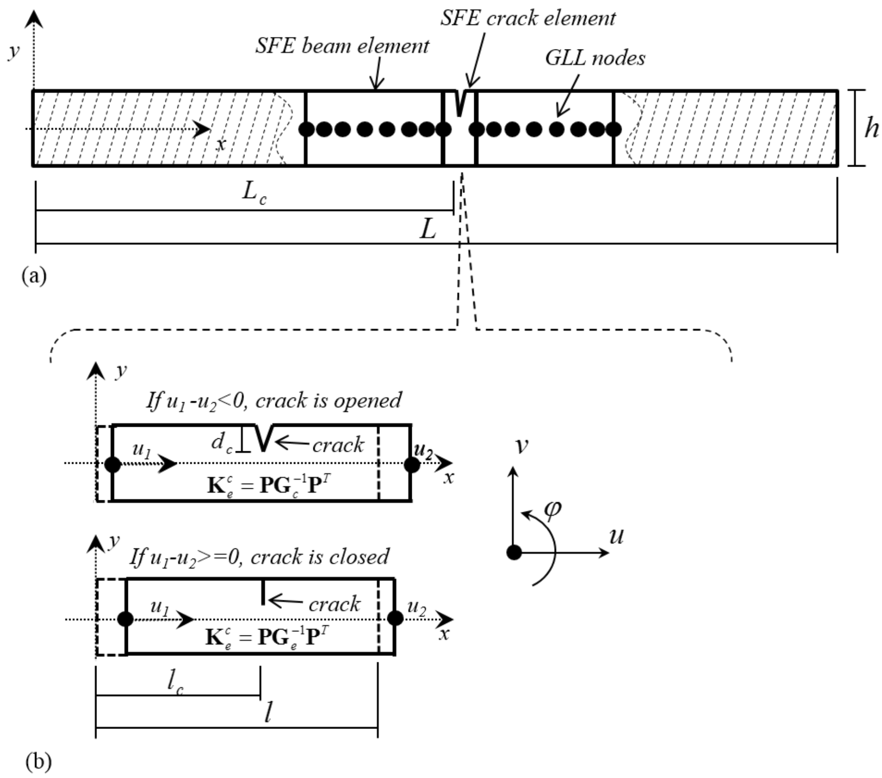

Figure 1. Schematic diagram of a SFE model for simulating a cracked beam, (a) discretization of a cracked beam; (b) two-node SFE crack element when the crack is opened and closed

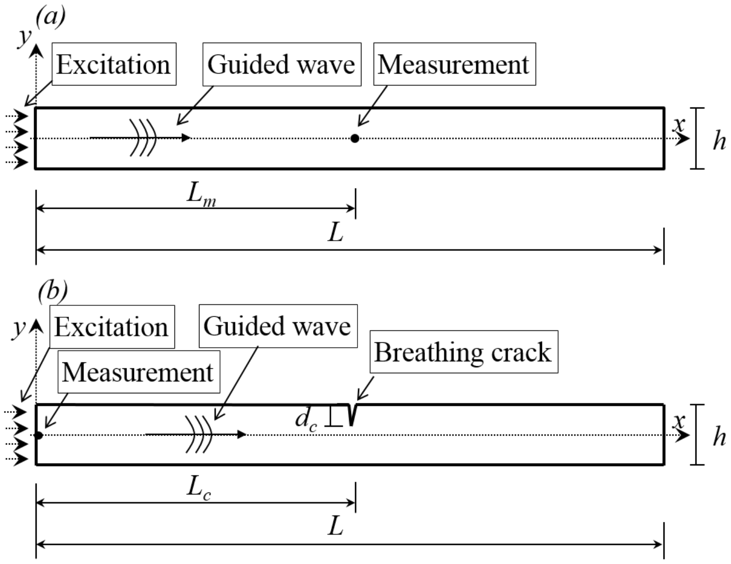

Figure 2. Schematic diagram of the SFE beam with (a) material and geometric nonlinearities; and (b) material, geometric and contact nonlinearities

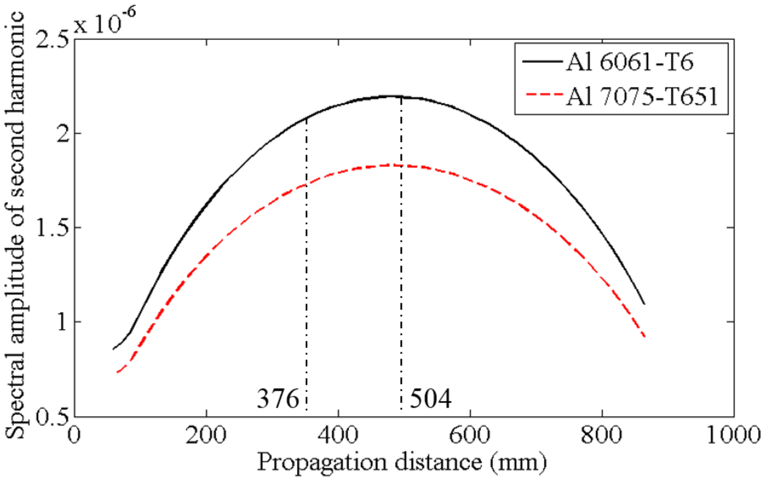

Figure 3. Spectral amplitude of second harmonic against propagation distance for Al 6061-T6 and Al 7075-T651

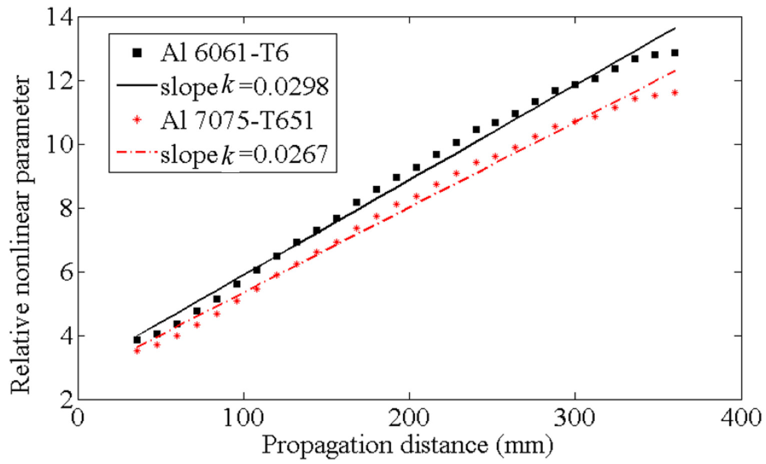

Figure 4. The relative nonlinear parameter β' calculated from the measured displacement against the wave propagation distance for the S_0 incident guided wave at 100 kHz

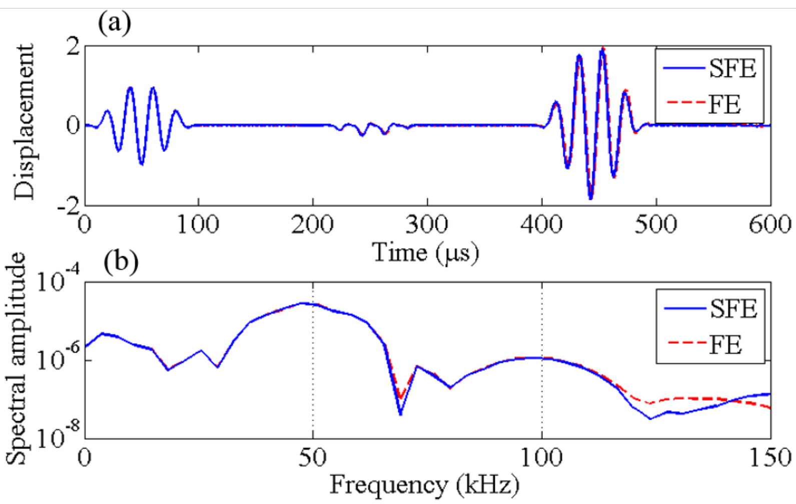

Figure 5. Comparison of SFE and FE simulated results in (a) time-domain; (b) frequency domain

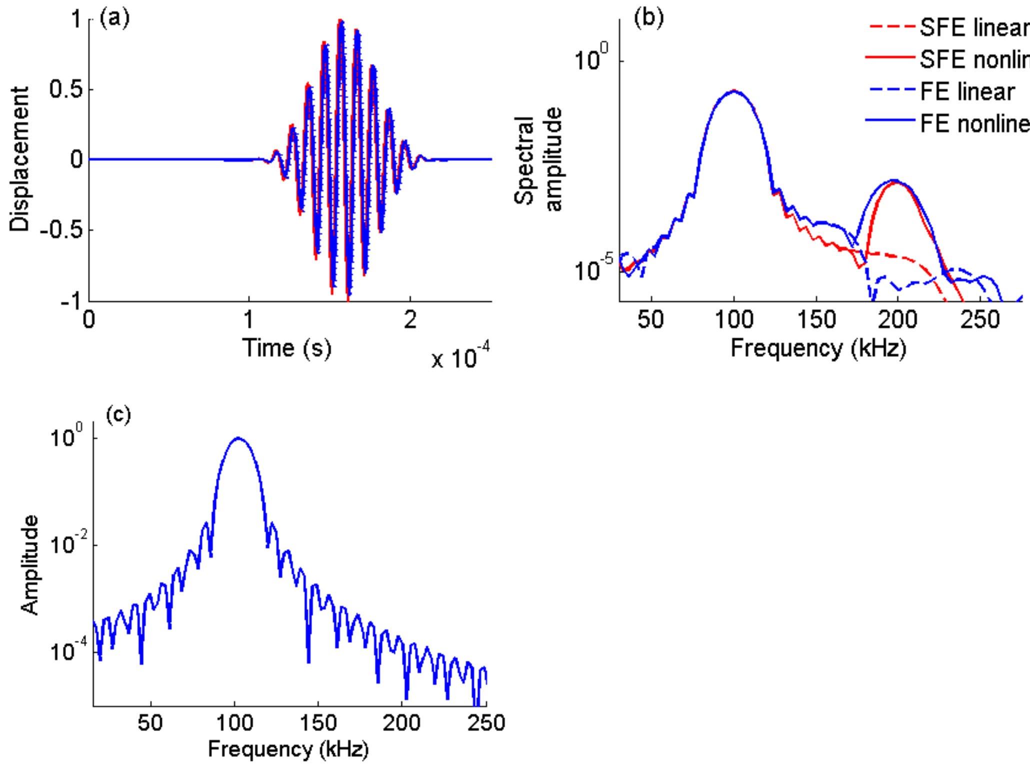

Figure 6 Comparison of SFE and FE simulations for linear and nonlinear perspective in terms of (a) time-domain; (b) frequency domain, and (c) the triggered signal in frequency domain

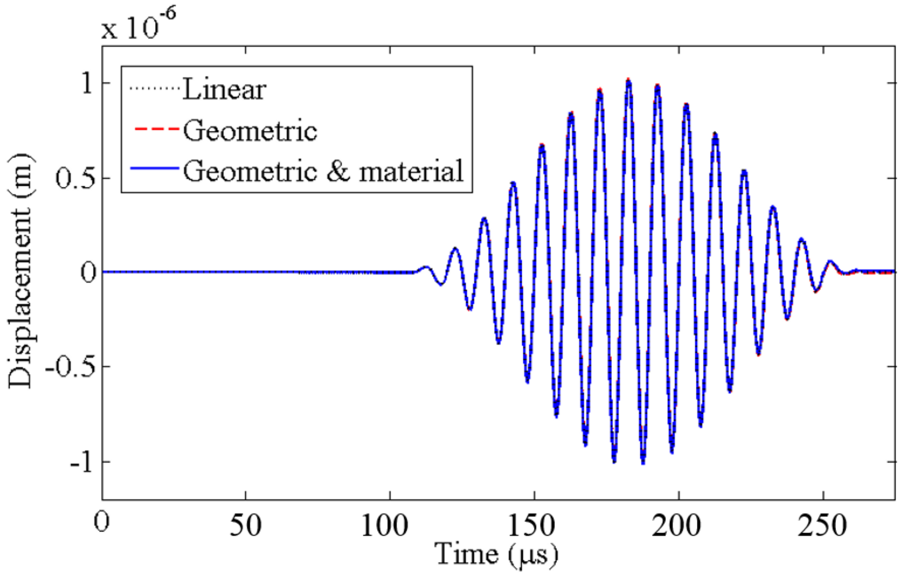

Figure 7. The calculated time-domain displacement response at L_m= 0.5 m for linear situation, and situations consider only geometric nonlinearity, and both material and geometric nonlinearities in the SFE simulation

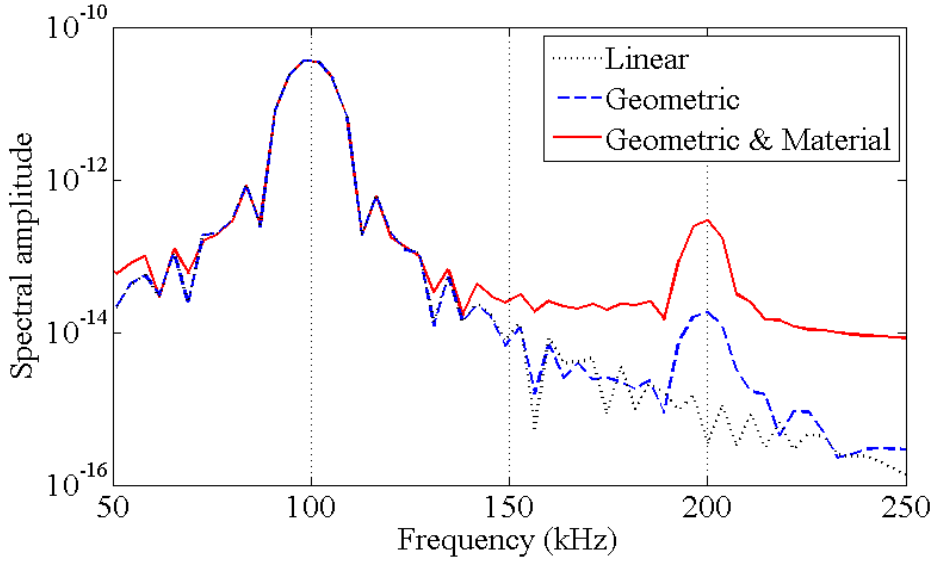

Figure 8. FFT of the calculated displacement responses at L_m= 0.5 m for linear situation, and situations consider only geometric nonlinearity, and both material and geometric nonlinearities in the SFE simulation

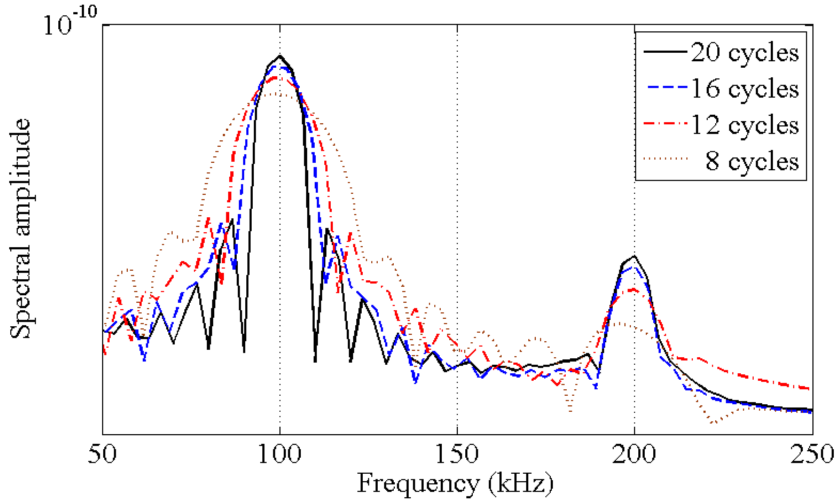

Figure 9. FFT of the calculated displacement responses at L_m= 0.5 m for different excitation cycles

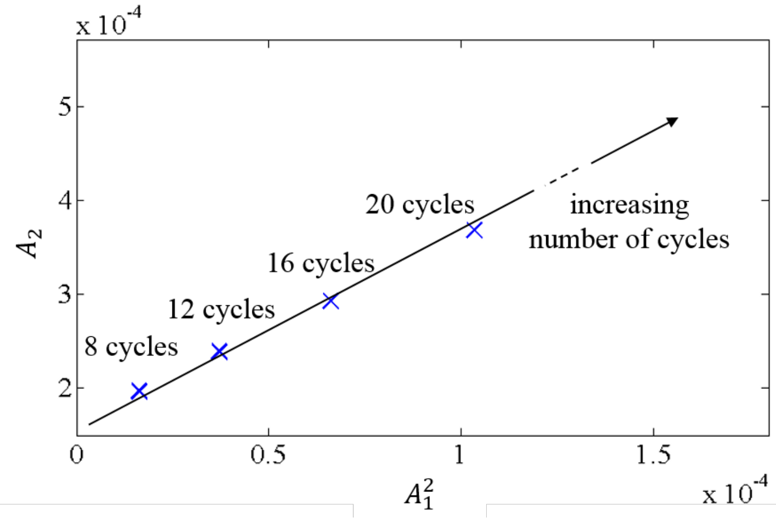

Figure 10. The second harmonic amplitude versus the fundamental amplitude for varying number of cycles of the excitation signal (solid line: analytical results; markers: SFE simulation results)

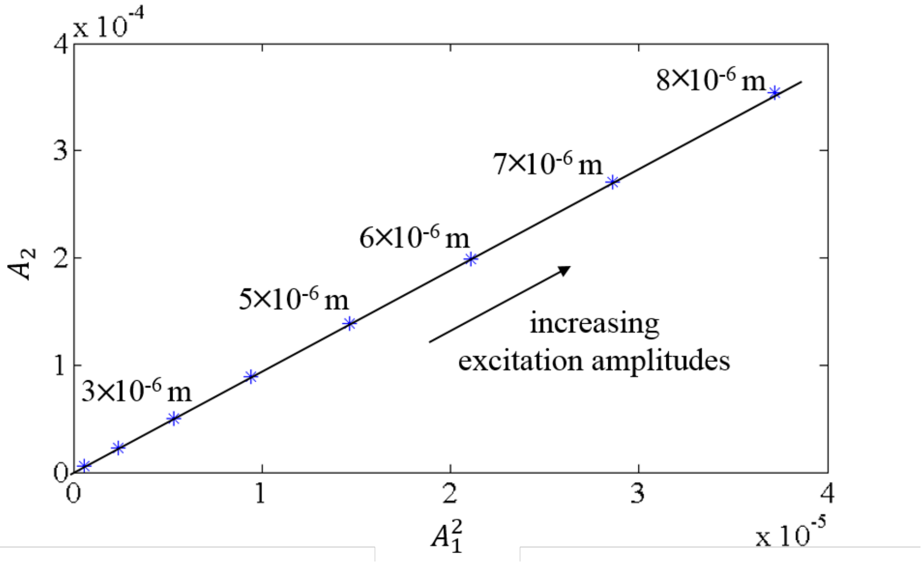

Figure 11. The second harmonic amplitude versus the fundamental amplitude for varying excitation amplitude (solid line: analytical results; markers: SFE simulation results)

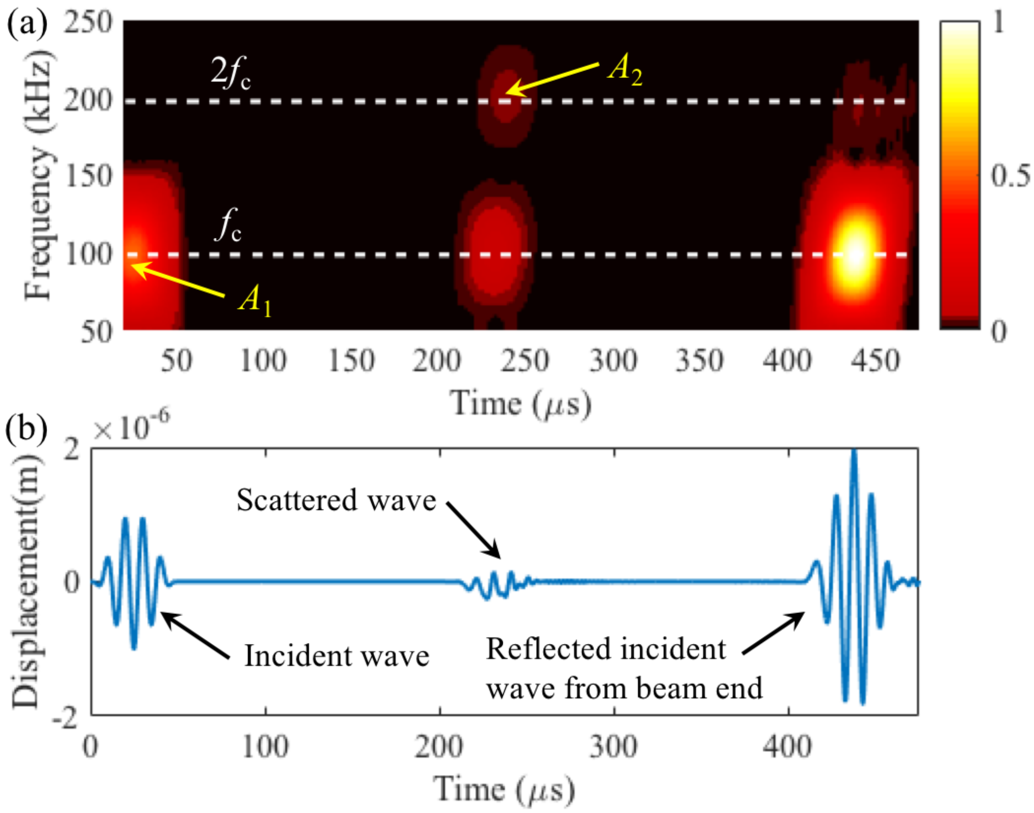

Figure 12. (a) Spectrogram obtained by STFT and (b) the corresponding time domain displacement response for a beam model with a crack having d_c =2.5 mm and L_c = 0.5 m

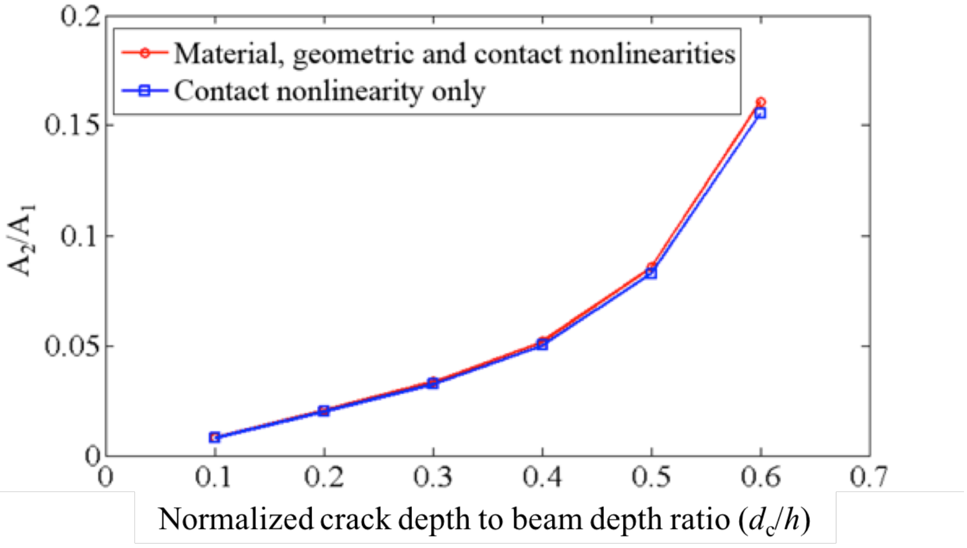

Figure 13. Normalized second harmonic amplitude of the displacement responses as a function of normalized crack to beam depth ratio (d_c/h)

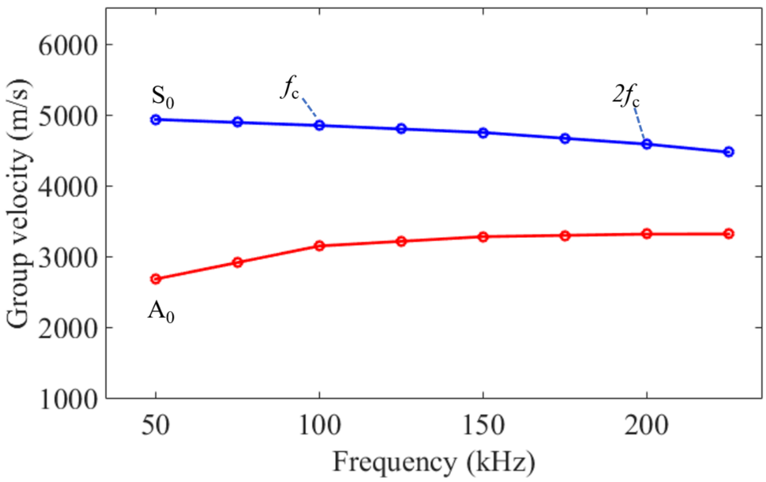

Figure 14. Group velocity dispersion curve for AI 6061-T6 beam

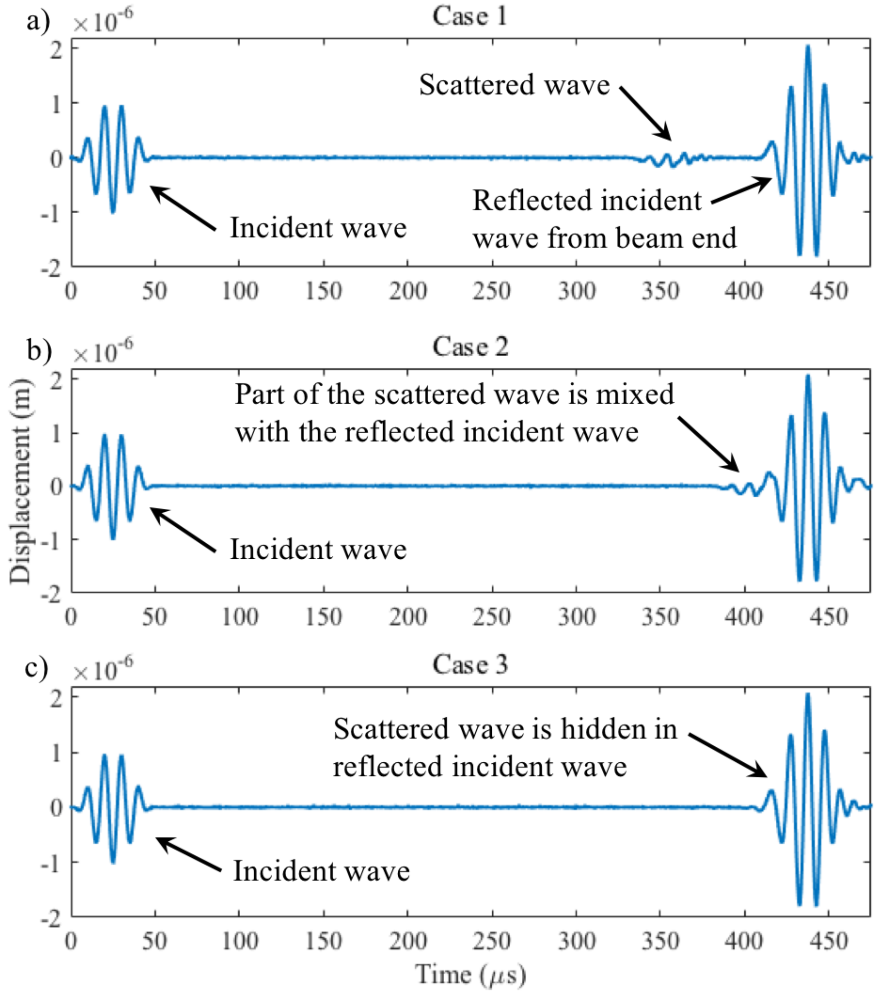

Figure 15. Measured time domain signal for a) Case 1, b) Case 2 and c) Case 3

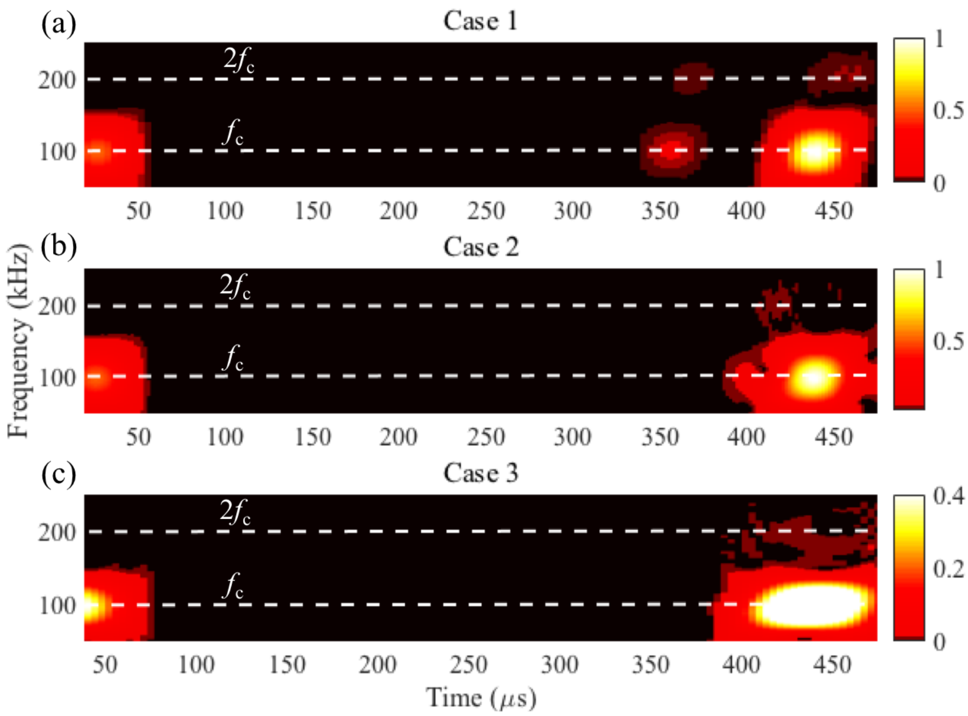

Figure 16. Spectrogram of the measured signals for a) Case 1, b) Case 2 and c) Case 3